Computing Ocean Surface Currents from GOCI Ocean Color Satellite Imagery Over the Bohai Sea, Yellow Sea, East China Sea and Sea of Japan

Jianfei Liu[1,*], William J. Emery[2], Miao Li[1], Chuan Li[1]

[1] Radio Oceanography Laboratory, School of Electronic Information, Wuhan University, Wuhan, P. R. China.

[2] Colorado Center for Astrodynamics Research, Department of Aerospace Engineering Sciences, University of Colorado, Boulder, Colorado, USA.

Corresponding author: Jianfei Liu (jfliu@whu.edu.cn)

Key Points:

- Routine ocean currents computed from sequential Geostationary Ocean Color Imager (GOCI) ocean color imagery over 5-year observation period.
- A 5-year mean and seasonal time-average flows reveal major currents in the area of interest.
- Observation of the evolution of Kuroshio meander over monthly and weekly time scales.

Abstract

One of the significant challenges in physical oceanography is getting an adequate space/time description of the ocean surface currents. One possible solution is the maximum cross-correlation (MCC) which we apply to hourly ocean color (OC) images from the Geostationary Ocean Color Imager (GOCI) over a 5-year long time period. Since GOCI provided a large number of MCC image pairs to process we introduce a new MCC search strategy to improve the computational efficiency of the MCC method saving 95.9% of the processing time. We also used a MCC current overlap method to increase the total spatial coverage of the currents, proving a 25.6% increase. A 5-year mean and seasonal time-average flows were computed for capturing the major currents in the area of interest (AOI). The mean flows investigate that the Kuroshio path, support the triple-branch pattern of the Tsushima Warm Current (TC) and reveal the origin of the TC. The evolution of the Kuroshio warm-core ring near the east coast of Japan is revealed by three monthly MCC composites. We capture the evolution of the Kuroshio meander over seasonal, monthly and weekly time scales. Three successive weekly MCC composite maps demonstrate how a large anticyclonic eddy, to the south of the Kuroshio meander, influences its formation and evolution in time and space. The unique ability to view short space/time scale changes in these strong current systems is a major benefit of the application of the MCC method to the high spatial resolution and rapid refresh GOCI data.

1 Introduction

Ocean currents represent a complex mixture of different types of aperiodic and periodic variability, ranging over wide ranges of horizontal size, velocities and time. These variations play significant roles in the global ocean circulation, and exert strong influence on ocean–atmosphere interactions [*Semtner*, 1995]. In addition, for practical reasons, ocean currents are also of great value in fishing, navigation, rescue, Tsunami warning [*Barrick*, 1979; *Georges et al.*, 1996] and ocean environmental protection from oil spills and harmful macro-algal blooms [*Abascal et al.*, 2009; *Ciappa et al.*, 2010]. Over the years, researchers have developed many instruments and techniques for estimating ocean surface currents. In situ, Eulerian observations are made at fixed positions and depth using mechanical currents meters or acoustic Doppler current profilers (ADCPs). Drifting buoys can be used to extract near-surface Lagrangian currents [*Ohshima et al.*, 2002], but they require the repeated reseeding of the buoys to continuously cover an area. Shore-based High Frequency (HF) radars [*Barrick et al.*, 1977; *Georges et al.*, 1996] are deployed near the coast to provide high temporal and spatial resolution real-time surface currents with a range of up to ~180 km off the coast from the backscatter of the radar signals. Space-based satellite altimetry measures sea surface height from which mesoscale geostrophic currents can be calculated, with the limitation that altimetry does not work well in shallow waters or near coastlines [*Roesler et al.*, 2013].

Ocean surface currents can be computed with the maximum cross-correlation (MCC) method from sequential thermal infrared (IR) [*Bowen et al.*, 2002; *Emery et al.*, 1986], ocean color (OC) [*Crocker et al.*, 2007; *Garcia and Robinson*, 1989; *Tokmakian et al.*, 1990; *Warren et al.*, 2016; *Yang et al.*, 2015] or synthetic aperture radar (SAR) imagery [*Emery et al.*, 2006; *Qazi et al.*, 2014]. Initially, *Emery et al.* [1986] verified that the MCC method works well to retrieve ocean currents from sequential Advanced Very High Resolution Radiometer (AVHRR) thermal IR imagery which many others have verified [*Dransfeld et al.*, 2006]. *Bowen et al.* [2002] demonstrated that it is better to apply the11 μm brightness temperature (BT) imagery instead of calculated sea surface temperature (SST) imagery which amplifies the noise in the SST estimation. And they further assessed the MCC currents as having a accuracy between 8 and 20 $cm\ s^{-1}$. *Garcia and Robinson* [1989] and *Tokmakian et al.* [1990] extracted ocean currents by applying the MCC method to Coastal Zone Color Scanner (CZCS) OC images. *Crocker et al.* [2007] computed ocean currents using OC imagery from NASA's Moderate Resolution Imaging Spectroradiometer (MODIS) and the Sea-viewing Wide Field-of-view Sensor (SeaWiFS). By combining BT and OC derived velocity fields, the total spatial coverage was increased by approximately 25%. *Yang et al.* [2015] applied the MCC method to a limited number of Geostationary Ocean Color Imager (GOCI) OC images for calculating the ocean surface currents and estimated the accuracy of the currents derived from various OC products. *Warren et al.* [2016] estimated the ocean currents from a relative small number of GOCI images using the MCC method over the Tsushima Strait. Comparisons between the MCC and HF radar currents indicate that the accuracy of the MCC velocities is on the order of 20 $cm\ s^{-1}$ and the blue-green OC derived MCC currents have a better performance than other OC products. *Qazi et al.* [2014] computed the ocean currents over the California Current System using 30-min-separation sequential C-band ERS-2 SAR and Envisat Advanced SAR (ASAR) imagery and compared the results with HF radar currents, which have lower magnitudes by ~11 $cm\ s^{-1}$. In a similar study of TerraSAR-X SAR imagery, *Emery et al.* [2006] computed coastal currents. All these studies validate that the MCC method is a successful feature tracking method for extracting ocean currents from various kinds of satellite imagery containing different ocean surface features.

In addition, the MCC method has also been verified as being effective in the observation of current structures of the Gulf Stream [*Emery et al.*, 1992], the California Current [*Kelly and Strub*, 1992; *Matthews and Emery*, 2009], coastal currents off the western coast of southern India [*Rajput et al.*, 2014], the Rio del Plata confluence zone [*Domingues et al.*, 2000], the East Australian Current [*Bowen et al.*, 2002; *Bowen et al.*, 2005], and the Tsushima Warm Current (TC) [*Warren et al.*, 2016]. In the area covered by GOCI, the Kuroshio Current (KC) is one of the major currents of the western boundary current region, which is a significant part of the circulation of the north Pacific as often discussed in the literature [*Andres et al.*, 2008; *Hidaka*, 1972; *Ichikawa and Beardsley*, 1993]. The GOCI sensor is in geostationary orbit and covers an area of $2500\ km \times 2500\ km$ providing eight images per day at hourly intervals [*Ryu et al.*, 2012]. Thus, using MCC with GOCI imagery can capture high temporal resolution mesoscale ocean currents variability, providing a new opportunity to capture changes in the KC and other currents.

In this paper, we use the MCC method with a new search strategy applied to sequential GOCI OC imagery over 5 years to routinely retrieve ocean currents. And we also combine the MCC currents derived from different OC products to increase the spatial coverage of the MCC currents. Using these high temporal sampling rate MCC velocity fields, we investigate the space/time variability of some of the major currents in the area of interest (AOI). The evolution of the Kuroshio warm-core ring (WCR) near the east coast of Japan is captured by the monthly MCC composites. The variability of the Kuroshio's path is revealed by seasonal, monthly and weekly MCC composite maps. We also demonstrate the anticyclonic eddies could influence the formation of the Kuroshio meander. These unique high spatial resolutions but short time interval MCC current maps provide a unique perspective on the space/time changes of this important major current system. This paper is organized as follows. Section 2 describes the GOCI OC products used and the AOI. Section 3 introduces the MCC method and several key parameters for running MCC along with a new search strategy to improve the computational efficiency of the MCC method. Section 4 discusses the total spatial coverage of the OC products, MCC fields and investigates the major currents in the AOI using a multi-year (5-year) mean and seasonal time-average flows. We also examine the variability of the Kuroshio's path and the evolution of the Kuroshio meander. Finally, a discussion and conclusions are provided in Section 5.

2 Data and AOI

GOCI, the world's first OC sensor in geostationary orbit, acquires data eight times per day in hourly separations from 00:15 to 07:45 GMT during the daytime. It has two near-infrared bands (745 and 865 nm) and six visible bands (412, 443, 490, 555, 660 and 680 nm). The coverage of GOCI, is shown in Figure 1 and covers $2500\ km \times 2500\ km$ with a spatial resolution of ~500 m at the center at $36^{\circ}N$ and $130^{\circ}E$. This area covers the Bohai Sea, the Yellow Sea, the East China Sea (BYECS), the Sea of Japan and a portion of the western Pacific to the south of Japan. The entire area covered by the GOCI sensor is selected as the AOI for the mesoscale ocean currents estimation and our subsequent current system investigation. There are several major currents in our AOI, such as the KC, the TC, the Taiwan Warm Current (TWC), the Tsugaru Warm Current (TSC), the Soya Warm Current (SY) and the Oyashio Current (OY). Many researchers used measurements from ADCPs, drifting buoys, HF radars and altimetry [*Andres et al.*, 2008; *Ebuchi et al.*, 2006; *Ichikawa and Beardsley*, 2002; *Ito et al.*, 2003; *Ito et al.*, 2014; *Takahashi and Morimoto*, 2013] or numerical models [*Kawamura et al.*, 2009; *Mitsudera et al.*, 2001] to investigate these currents.

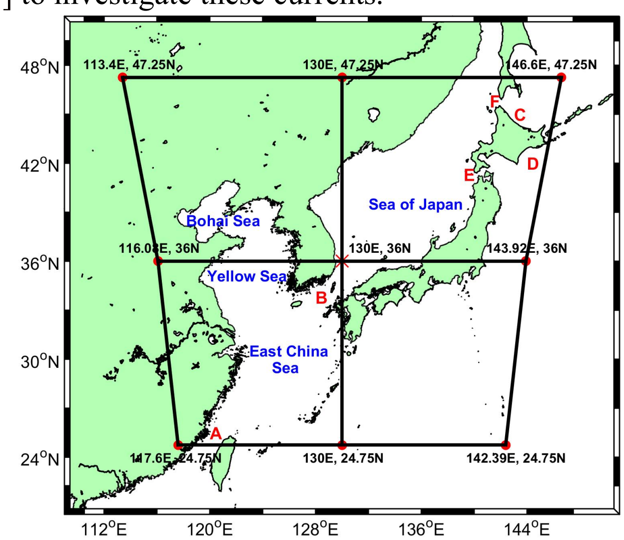

Figure 1. Area of interest in the solid line box is $2500\ km \times 2500\ km$ at a center of $36^{\circ}N$ and $130^{\circ}E$, including the Bohai Sea, the Yellow Sea, the East China Sea, the Sea of Japan and a portion of the western Pacific to the south of Japan. Red marks A, B, C, D, E and F represent the Taiwan Strait, Tsushima Strait, Sea of Okhotsk, eastern shore of Japan Tsugaru Strait and Soya Strait, respectively.

The 5-year long GOCI Level-2 data, from Jun. 1, 2011 to May. 31, 2016, were obtained from the NASA ocean data website (https://oceandata.sci.gsfc.nasa.gov/). The Level-2 OC products are cloud free data, which are atmospherically, radiometrically and geometrically corrected. These datasets consist of a series of OC products, including the chlorophyll-a concentration (Chl) calculated using the OCI algorithm presented by *Hu et al.* [2012], the diffuse attenuation coefficient at 490 nm (Kd490) and the remote sensing reflectance (Rrs(λ) where λ is the wavelengths from 412 nm to 680 nm), which are all derived from the multiple GOCI bands. Due to the spatial image discontinuities of GOCI data, especially for 412 and 490 nm [*Wang et al.*, 2013; *Warren et al.*, 2016], and the acquisition and processing algorithms, the OC products of 412 and 490 nm are not considered in this paper. Previous study has shown that the green 551 channel is best suited for the ocean current estimation using the MCC method [*Yang et al.*, 2015]. In addition, the Chl product is the most often used OC product for estimating ocean currents, as shown by *Crocker et al.* [2007], *Yang et al.* [2015] and *Warren et al.* [2016]. In this paper, the OC products, Chl and Rrs555, have been selected as the datasets for the ocean current retrieval with the MCC method.

3 Method

The MCC method is an automated procedure that identifies a MCC between the features of two sequential images [*Crocker et al.*, 2007; *Emery et al.*, 1986; *Emery et al.*, 1992]. The first image is divided into a number of template tiles and each template window will be searched for within a search window in the second image (see Figure 2). The feature displacement of the two images is defined as the location of the MCC between the template window in the first image and the matching template window in the search window in the second image. This defines the velocity vector with an origin at the center of the template window in the first image and the end point at the location of MCC in the search window in the second image. The sea surface current vector is computed by dividing the displacement vector by the time interval of the two images.

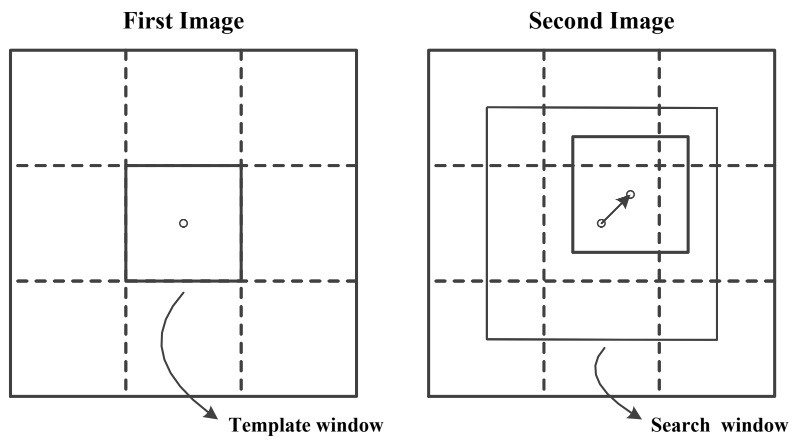

Figure 2. Sketch of the MCC algorithm. Run MCC with two sequential OC imagery with a spatial resolution of Δr at T_1 and T_2, respectively. The time interval is defined as $\Delta T = T_2 - T_1$.

A raw MCC velocity field contains vectors at every grid point with different cross correlations. To eliminate the unreliable vectors, several filters have been proposed. First, a minimum correlation cutoff is set to 0.8 and the vectors with poor cross correlations are removed. Second, a next neighbor filter is applied to ensure spatial coherence. For a target vector, all the adjacent vectors need to agree within a specified magnitude. In this paper, we require that both u and v components of four neighborhood vectors are within $10\ cm\,s^{-1}$ compared with the target vector. More details of this procedure are described in [*Bowen et al.*, 2002; *Crocker et al.*, 2007].

The main parameters in the MCC method are the time interval, the size of the template window and the size of the search window. These issues are discussed in detail in the following sections.

3.1 Time Interval

The MCC method is a feature tracking method for sequential images and the velocity resolution of the MCC velocity field depends on the spatial resolution Δr of the imagery and the time interval ΔT between the two images

$$v_{res} = \frac{\Delta r}{\Delta T} \tag{1}$$

Compared with the satellite imagery from AVHRR, MODIS and SeaWiFS, the GOCI imagery has a higher spatial resolution of ~500 m instead of ~1.1 km and shorter time intervals, as short as 1 h. This indicates GOCI imagery derived currents can have greater velocity resolution. In their study, *Crocker et al.* [2007] proved that the MCC method can produce consistent currents off the US. West Coast from OC imagery with time intervals from 3-24 h. The GOCI provides eight images each hour from 00:15 to 07:45 GMT during the daytime, while MODIS and SeaWiFS only can provide global coverage once during the daytime. The time interval ΔT between the sequential GOCI images can either be 1-7 h or 17-24 h. The resulting velocity v_{res} against ΔT is shown in Table 1, and is inversely proportional to ΔT. Longer time intervals imply better velocity resolutions of the MCC outputs. In addition, for ΔTs above 3 h, v_{res} is less than 5 $cm\ s^{-1}$, making it possible to better resolve small features.

For the AOI, GOCI can provide constant data coverage with high spatial and temporal resolutions. The number of sequential image pairs N per day against time interval is shown in Table 1. There are routinely 64 pairs of imagery with start times on the same day, which can produce 64 MCC velocity fields from one OC product. As the different OC products may depict different ocean surface patterns, the MCC currents derived from these different OC products may have different spatial characteristics, which can be combined over time to improve the spatial coverage of the MCC vector fields. The GOCI OC derived MCC velocity fields are rapidly sampled which makes it possible to capture the variability of the mesoscale currents that have been derived from other OC imagery like MODIS and SeaWiFS. The rapid sampling rate of the GOCI derived currents makes it possible to investigate tidal currents over 1 h or longer time periods.

Table 1. The velocity resolution, number of sequential image pairs per day and the search range of the MCC with GOCI imagery separated by 1-7 h and 17-24 h.

$\boldsymbol{\Delta T}$ (h)	1	2	3	4	5	6	7	17	18	19	20	21	22	23	24
$\boldsymbol{v_{res}}$ ($\boldsymbol{cm\ s^{-1}}$)	13.89	6.94	4.63	3.47	2.78	2.31	1.98	0.81	0.77	0.73	0.69	0.66	0.63	0.60	0.58
$\boldsymbol{N}$	7	6	5	4	3	2	1	1	2	3	4	5	6	7	8
$\boldsymbol{S_R}$	10	19	29	38	47	57	66	160	169	078	188	197	206	216	225

3.2 The Size of the Template and Search Windows

The template window should be large enough to contain enough pixels to compute statistically significant correlations. However, if the size of the template window is too large, this will smooth out the structure of the resulting flow field and degrade the spatial resolutions of the MCC currents. Considering the above factors, we selected a template window size of 44×44 pixels ($22\ km \times 22\ km$), which was also used by *Emery et al.* [1986], *Crocker et al.* [2007] and *Warren et al.* [2016], and it proved to be effective.

Normally, the spatial resolution of the MCC velocity field corresponds to the size of the template window. We developed a multi overlap method to obtain various spatial resolutions of the MCC currents. The size of the template window determines the spatial resolution of the MCC currents because the start of the vector is the center of the template window in the first image. Hence, if the images are divided into template tiles with overlap, the number of template tiles is increased. Then the spatial resolution of the MCC currents is also improved. By employing this method, we obtained various spatial resolutions of the MCC currents. However, we also note that this method also increases the processing time of the MCC searches. As a result, we used an overlap of 22 pixels between continuous template windows improves the spatial resolution of the current vector to 22×22 pixels ($11\ km \times 11\ km$).

The search window in the second image should be large enough to accommodate the maximum expected velocity. *Ito et al.* [2003] found the maximum subtidal current of TSC is about 130 $cm\ s^{-1}$, while the maximum currents speed of the KC is about 100 $cm\ s^{-1}$ [*Takahashi and Morimoto*, 2013]. *Warren et al.* [2016] selected a maximum velocity of 100 $cm\ s^{-1}$ to estimate the TC with the MCC method in the Tsushima Strait. For higher expected velocities, the search range of the MCC increases. Based on these considerations, the maximum expected velocity is specified as $V_{max} = 130\ cm\ s^{-1}$. Hence, the search range of the MCC method can be computed as

$$S_R = \left[\frac{V_{max}\Delta T}{\Delta r}\right] + 1 \tag{2}$$

where $[\cdot]$ represents the integer part of a number. The search ranges are linear relative to the time interval between the sequential imagery. From Table 1, we can find that the search range gains distinctly as the time interval increases. For our MCC velocities, the size of the search window should be $2(S_R + 22) \times 2(S_R + 22)$ pixels.

3.3 Merging MCC Currents Computed from Different OC Products

The MCC method fails when the observation area is populated with weakly trackable features or the optical images are covered with persistent clouds, which result in missing OC data [*Bowen et al.*, 2002]. From Figure 3a-d, approximately 71% of the data in the AOI is missing mainly due to cloud cover. In addition, sparsely covered cloudy pixels also can cause a degradation of MCC derived currents. In the southeast of the AOI, there is always some cloud cover, resulting in missing OC data. The missing data in the template window will decrease the cross-correlation coefficient and cause unreliable vectors [*Bowen et al.*, 2002; *Warren et al.*, 2016]. Figure 3e shows the ocean currents derived from the two individual hourly OC products. There are clearly fewer vectors in the southeast of the AOI because of the persistent cloud cover and weak surface feature patterns. Considering the areas east of Taiwan, the Tsushima Strait, west of Sea of Japan, east of Japan and south of the AOI, the sea surface features exhibit weak patterns. Hence, there are almost no vectors in these areas. As shown in Figure 3e, the China Coastal Current flows southward along the mainland China coast and the TWC flows northward along the Taiwan coast. The TC flows through the Tsushima Strait and the Yellow Sea Warm

Current (YSWC) flows northward. The Bohai Coastal Current is also depicted by this one-hourly MCC velocity field, flowing northward into the Yellow Sea. About 78% of u- and v- components of the corresponding vectors are coincident (Figure 3f) while about 20% of the components are within the velocity resolution. The RMS differences of the u- and v- components between the two velocity fields are 7.54 and 8.20 $cm\ s^{-1}$, respectively. These results indicate that there is high similarity between the two velocity fields.

Previous studies have proven the MCC method performs well with Chl and Rrs555 products for the computation of ocean currents [*Warren et al.*, 2016; *Yang et al.*, 2015]. In addition, the two distribution curves in Figure 3f indicate the high similarity of the two MCC velocity fields and that they have almost the same accuracy order. As the two velocity fields show a difference in their spatial distributions, the two separate velocity fields can be fused to improve the spatial coverage. Consider M velocities in the same pixel derived from M GOCI OC products, the fused velocity can be calculated as

$$\begin{cases} u_m = \sum_{i=1}^{i=M}(c_i u_i) / \sum_{i=1}^{i=M}(c_i) \\ v_m = \sum_{i=1}^{i=M}(c_i v_i) / \sum_{i=1}^{i=M}(c_i) \end{cases} \quad \textbf{(4)}$$

where u_i (v_i) and c_i are the u- (v-) component and MCC derived from the ith OC product, respectively.

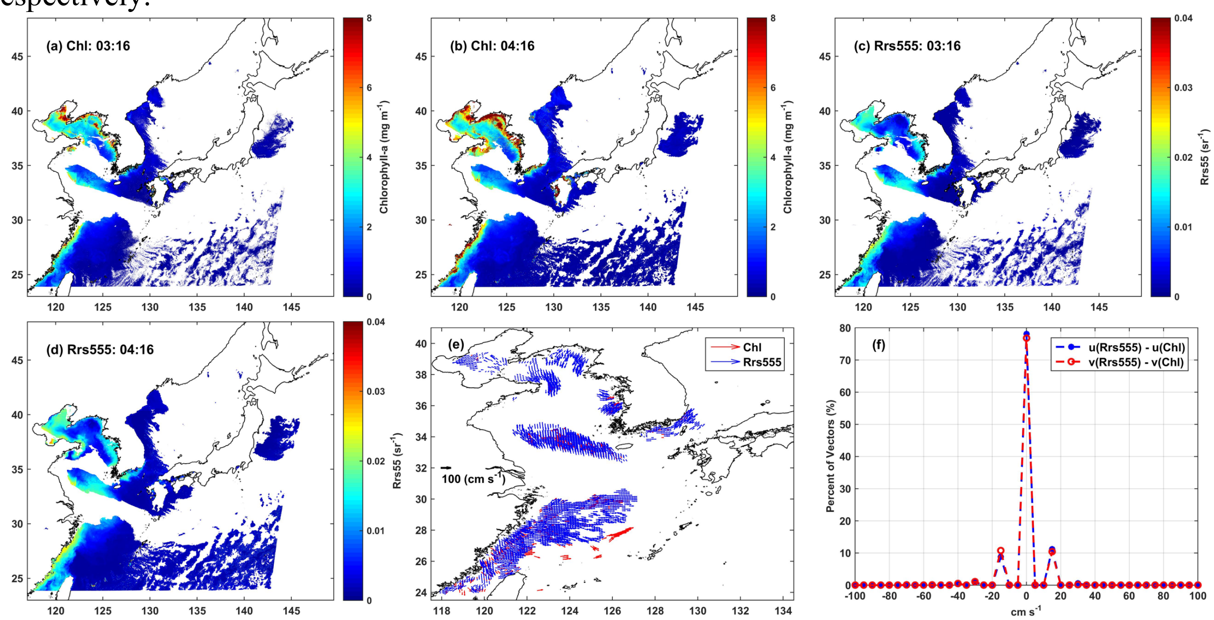

Figure 3. Sequential GOCI images of **(a)** Chl at 03:16 UTC, **(b)** Chl at 04:16 UTC, **(c)** Rrs555 at 03:16 UTC and **(d)** Rrs555 at 04:16 UTC on Feb. 9, 2016. **(e)** The velocity fields were computed from the Chl images (a) and (b) (red arrows), and Rrs555 images (c) and (d) (blue arrows). The total number of the vectors from the Chl and Rrs555 is 1,123 and 2,203, respectively, while the number of the corresponding vectors of the two velocity fields is 1,010. **(f)** Histogram comparison of the corresponding vectors derived from Chl and Rrs555. The RMS differences of the u- and v- components between the two velocity fields are 7.54 and 8.20 $cm\ s^{-1}$, respectively.

3.4 MCC Current Composites

Normally, the MCC velocity fields have different spatial and temporal coverage due to the time intervals, the size of the search windows, vector filtering, cloud cover and weakly trackable features. By compositing over several days, we can reduce these influences and increase the spatial coverage of the MCC currents. To routinely extract ocean currents using the MCC method from GOCI OC products, there are 64 velocity fields per day for each OC product; each having time spans of 1-7h or 17-24 h. Due to the high temporal resolution of the MCC currents, we can make MCC calculated composite current maps for intervals as short as one day. The composite MCC velocity fields are mapped to a 44×44 pixel ($22\ km \times 22\ km$) grid, which is also selected by *Crocker et al.* [2007] and *Matthews and Emery* [2009].

4 Evaluation of the Routine MCC Implementation

4.1 Spatial Coverage of GOCI Data

As mentioned earlier, the satellite data quality has a significant influence on the MCC method. The cloud cover degrades the quality of the GOCI data, especially in terms of its spatial distribution. Thus, the total spatial coverage of the GOCI OC products over the observation period was calculated to analyze the spatial distribution statistics of the GOCI data. This will constrain the analysis of the spatial distribution of the MCC current fields. We show the overall spatial coverage distribution of the two OC products over the observation period in Figure 4. The spatial distributions of these two OC products are similar, but there are measurable differences in percentage values. In the AOI, both OC products have a data coverages above 15% in most areas. About 20% of data coverage around Taiwan and 22% of data in the path of the KC. There are clearly fewer data (~2%) west of the Bohai Sea, Yellow Sea and the western edge of the AOI for both OC products. The Rrs555 has a higher percentage (~35%) along the Russian coast, south of Japan, Korea and in area A than that of the Chl products (~25%).

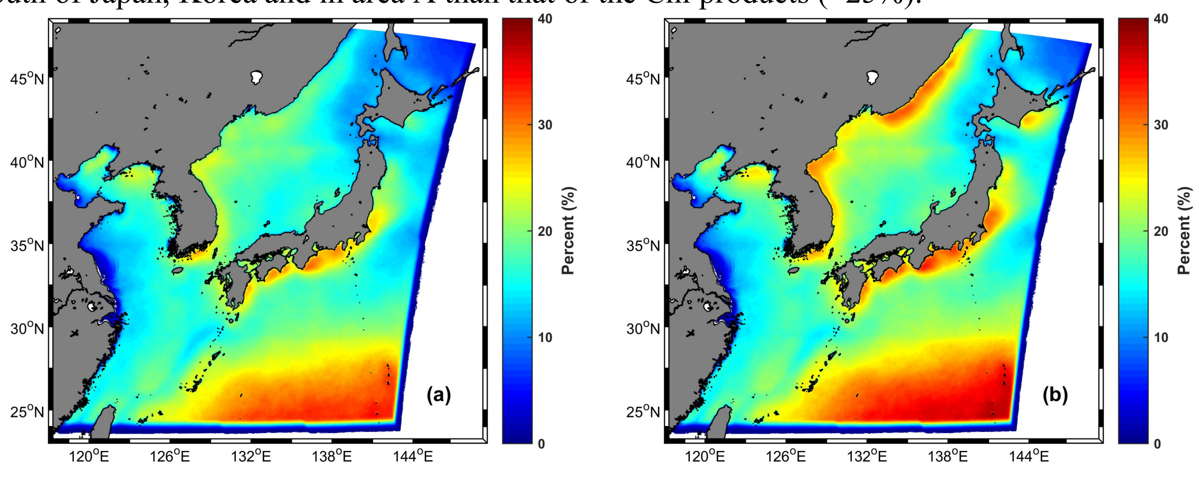

Figure 4. Overall spatial distribution of the two GOCI OC products, **(a)** Chl and **(b)** Rrs555, over the observation period. The color bar represents the percentage of data coverage.

The area with the greatest data coverage should have a higher probability of producing more MCC vectors. But the MCC method also requires surface features to track and the temporal continuity of the data to provide sequential imagery. Though there is always better coverage along the coast except west of the AOI; the southern area does not produce as many MCC vectors due to persistent cloud cover and the dominance of weak surface feature patterns. But the spatial distribution of the filtered GOCI data indicates areas of persistent cloud cover in the AOI.

4.2 New Search Strategy for the MCC Method

The MCC method calculates the cross-correlation coefficient between the template window in the first image and the matching template window within the search window in the second image. The end point of the MCC current is determined by locating the correlation maximum in this search window. This means that for each template window's matching process, approximately $2S_R \times 2S_R$ cross-correlation calculations are carried out. A larger S_R implies far more computational time, since the search times are about four times the square of S_R. The larger S_R, the greater the number of computations, and the increased processing time. As our AOI is large covering 5567×5685 pixels, which covers approximately 32,000 template tiles (with an overlap of 22 pixels). To able to efficiently process this very large data set, we propose a new search strategy to improve the search efficiency of the MCC method. This new search procedure is: First, define a skip range, which is the number of pixels skipped between the two sequential windows in the MCC search procedure. This step will decrease the search steps. Thus, we compute the MCC maximum at this coarse search step. Second, we define a region search range (RSR), which is the search range around the coarse MCC peak to get a more accurate MCC maximum. Third, we also define a reference velocity V_R, which is accurate enough for our ocean current retrievals and is also consistent with the velocity search step of the new search strategy. The skip range can be calculated as

$$\text{skip} = \begin{cases} \left[\frac{V_R}{v_{res}}\right] - 1 = \left[\frac{V_R \Delta T}{\Delta r}\right] - 1\,, skip \geq 2 \\ 0\,,\ skip \leq 1 \end{cases} \tag{3}$$

and the RSR is set to the same value as the skip to ensure the computation of the more precise MCC maximum without decreasing the velocity resolution of the MCC currents. For lower reference velocities, the skip values calculated by the above equation may be less than 0 and then the skip value is set equal to 1, and the new method has the same performance as the conventional MCC method. In this situation, we set the skip value to 0.

The proposed new search strategy significantly improves the computational efficiency of MCC by setting a reasonable reference velocity V_R. We performed several different experiments, where we set V_R to 3, 5, 10 and 14 $cm\ s^{-1}$, respectively, to validate the efficiency of the new search strategy. First, we present the skip range against time interval for different reference velocities in Table 2. This table shows that at small time intervals, the "skip" results are the same as MCC without a skip. As can be seen in Figure 5a, the computational time of the conventional method significantly increases when the time interval increases. The computational time decreases as V_R increases from 3 to 14 $cm\ s^{-1}$, saving 79.7%, 95.9%, 97.6% and 97.1% of the average time relative to the conventional search method when ΔT is above 17 h, respectively. However, when V_R is 14 $cm\ s^{-1}$, the computational efficiency does not improve due to the gain of the RSR for the more accurate MCC compared to that for the situation when V_R is 10 $cm\ s^{-1}$. Second, with a larger reference velocity search, the number of the search steps obviously decreases, but the MCC maximum is in the lower sampling region, which increases the probability of missing the correct MCC peak, resulting in an incorrect MCC velocity. These vectors may be filtered in the post-processing procedure resulting in the probability that the total number of vectors is reduced. In Figure 5b we can see that, when V_R is smaller (3 or 5 $cm\ s^{-1}$), the total number of vectors decreases an average percentage of 1.7% and 6.3%, respectively, while if V_R is larger (10 or 14 $cm\ s^{-1}$), the total number of vectors decreases an average percentage of 21.6% and 32.2%, respectively. Third, considering the influence of V_R on the accuracy of the MCC currents, as shown in Figure 5c, where with larger reference velocities (10 or 14 $cm\ s^{-1}$), the RMS error is much larger, as large as 8.22 $cm\ s^{-1}$, while with lower reference velocities (3 or 5 $cm\ s^{-1}$), the RMS error is below 2.00 $cm\ s^{-1}$.

All in all, the selection of V_R is a balance between computational time, the number of missing vectors and the accuracy of the MCC velocities. In this paper, V_R is set to 5 $cm\ s^{-1}$ to ensure the acceptable accuracy of our current estimates, minus the missing vectors and a relatively lower computational expense.

Table 2. The skip value against time interval when V_R is set to 3, 5, 10 and 14 $cm\ s^{-1}$.

$\Delta \boldsymbol{T}$ (h)	1	2	3	4	5	6	7	17	18	19	20	21	22	23	24
$\boldsymbol{V_R = 14\ cm\ s^{-1}}$	0	0	2	3	4	5	6	16	17	18	19	20	21	22	23
$\boldsymbol{V_R = 10\ cm\ s^{-1}}$	0	0	0	0	2	3	4	11	11	12	13	14	14	15	16
$\boldsymbol{V_R = 5\ cm\ s^{-1}}$	0	0	0	0	0	0	0	5	5	5	6	6	6	7	7
$\boldsymbol{V_R = 3\ cm\ s^{-1}}$	0	0	0	0	0	0	0	2	2	3	3	3	3	3	4

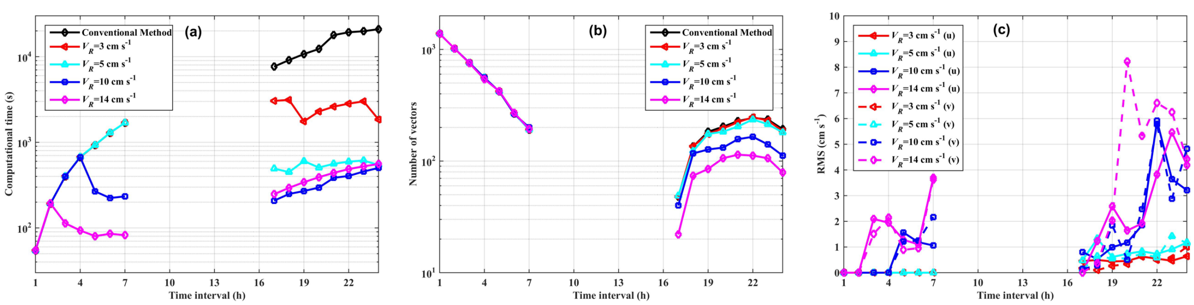

Figure 5. Sixteen Chl images on May 21 and 22, 2015 are selected as the inputs of the MCC method to evaluate the performance of the new search strategy for their large volume of data. All the experiments are completed using C code, on a Red Hat Enterprise Linux 6.8 computer with a CORE i7 processor, 3.40 GHz CPU and 16 GB of memory. All the results are normalized by the number of pairs N. Comparisons of the estimate performance **(a)** the computational time, **(b)** the number of vectors and **(c)** the RMS errors between the conventional search method and the new search method against the time interval when V_R is 3, 5, 10 and 14 $cm\ s^{-1}$, respectively.

4.3 Routine MCC Results

Using the new search strategy, we can easily process the MCC ocean surface currents from all of the available GOCI data over the observation period and our AOI. The total number of monthly and seasonal Chl and Rrs555 derived MCC vectors in these observation periods is shown in Figure 6. The strong seasonal differences in the number of vectors are mainly due to changes in the general cloud cover in our AOI. These seasonal changes also reflect changes in the nature of the trackable surface features. Here, a comparison of the results derived from the two OC products is used to assess the performance of the MCC method from the two different OC products. There are always more vectors in the spring months due to the seasonally lower cloud cover in the AOI. It's clear in Figure 6b that the total number of vectors has a definite seasonal trend, with spring having more vectors while winter has the fewest number of vectors. The total number of Chl and Rrs555 derived MCC vectors over the observation period is 4,186,605 and 4,325,622, respectively. In addition, a seasonal bias was revealed, the percentage of the total number of vectors derived from Chl and Rrs555 from winter to fall is 8.3%, 42.7%, 27.2%, 21.8% and 9.0%, 41.8%, 26.5%, 22.7%, respectively. These results indicate that there are more vectors in spring, fewer in summer and fall, and the fewest in winter.

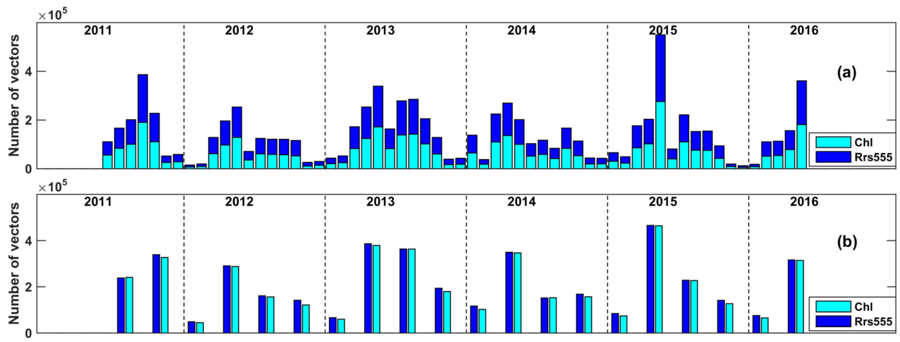

Figure 6. The total number of MCC vectors per **(a)** month and **(b)** season over the observation period derived from Chl and Rrs555 imagery. Winter is Dec., Jan. and Feb.; spring is Mar., Apr. and May.; summer is Jun., Jul. and Aug.; fall is Sep., Oct. and Nov..

Figure 7a-b show the number of daily composites over the observation period (1827 days) with a mean number of 157. There are 50 days producing no vectors and 137 days having number of vectors less than 20. 41.3% of the days have vectors less than 100. Figure 7c-d display the number of 7-day composites over the observation period (260 weeks) with a mean number of 685. There is no day with vectors less than 20. Most of the days has vectors around 600. Hence, in order to get a higher spatial coverage of the currents, we consider the 7-day MCC composites in this paper.

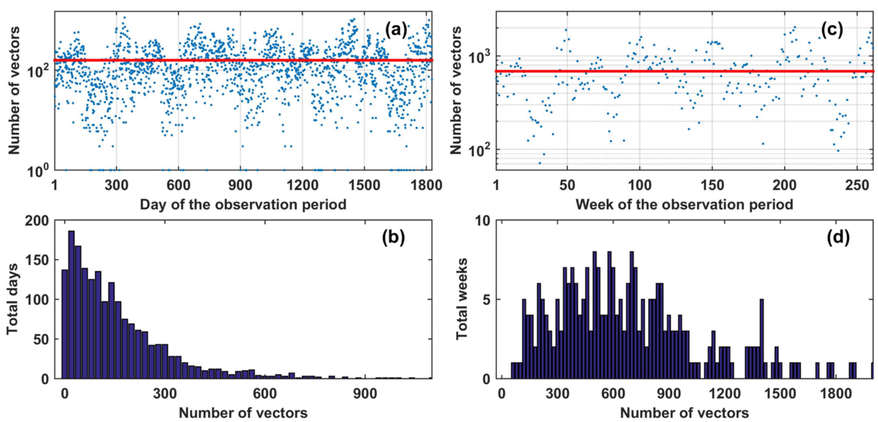

Figure 7. (a) and **(c)** Number of the daily and 7-day composite vectors over the observation period, respectively. Number of vectors in (a) is with a bias of 1 to avoid the zero value. The red lines are the mean number of vectors. **(b)** and **(d)** Distribution of number of the daily and 7-day composite vectors, respectively.

A comparison of the number of 7-day MCC composites is made between the Chl and Rrs555 derived currents. Even southeast of the AOI there is a high coverage percentage of the

OC data over the observation period (Figure 4); this area is always sparsely contaminated by clouds, resulting in fewer MCC vectors. It is shown in Figure 8a-b, that the total number of vectors southeast of the AOI is reduced relative to other areas. As shown in Figure 8a-b, the number of vectors derived from the two OC products are significantly different. For Chl derived currents, there are more vectors in the Sea of Japan, Tsushima Strait, east of Taiwan and along the Japan coast, while the Rrs555 MCC velocity fields have a rather more vectors in the BYECS and also in the Taiwan Strait. As displayed in Figure 8c, by fusing the two OC velocity fields, the total spatial coverage of the MCC velocity fields increases by approximately 25.6%, especially in the BYECS, the Taiwan Strait, the Tsushima Strait and along the Japanese coast. Compared with the altimetry derived currents, the MCC currents have higher temporal resolution [*Matthews and Emery*, 2009].

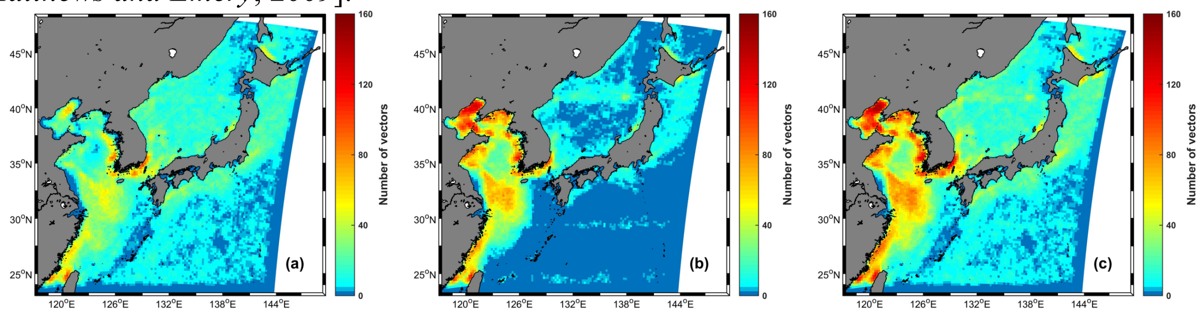

Figure 8. Number of 7-day MCC composites from **(a)** Chl imagery, **(b)** Rrs555 imagery and **(c)** the combination of the two OC imagery.

5 Results

5.1 Multi-year Mean MCC Currents

The MCC derived currents from the GOCI OC imagery were averaged over the 5-year observation period using the 7-day MCC composites derived from the merged Chl and Rrs555 derived currents. This is the first time that five years of GOCI images were applied to compute the ocean currents using the MCC method. The mean flows have an excellent spatial velocity coverage and are shown here in Figure 9a. Thanks to the large area coverage of the GOCI sensor, several major currents are included in the AOI.

The KC, the strong and persistently northward-flowing ocean current, is the most significant current in the AOI. The Kuroshio path, is approximately 2,400 km long with a width that varies from 100 km to 150 km. The current speed of the KC varies from 50-85 $cm\ s^{-1}$. Within the AOI, the KC starts east of Taiwan, then passes the Ryukyu Islands and Honshu, and flows along the Japanese coast, arriving at the southeast point of Hokkaido where it merges with the OY (also observed in area D). The OY, is a southward current from the Okhotsk Sea, which joins the KC to form an easterly flow known as the Kuroshio Extension. The TWC flows northward along the Taiwan coast with a current speed of 7-50 $cm\ s^{-1}$ and it splits into two parts around $26.5^{\circ}N$, one flows northward into the East China Sea and one flows northeastward merging with the KC. The China Coastal Current flows southward along the mainland China coast with a current speed around 10 $cm\ s^{-1}$ and a width about 50 km. In addition, the TC is also clearly depicted in Figure 9a (in area B), flowing through the Tsushima Strait. The origin of the TC may come from two different sources: the first considers the TC as a northward branch of the KC [*Nitani*, 1972] and the other considers the TWC as the origin of the TC [*Beardsley et al.*, 1985]. Our MCC currents support the KC branch theory. The KC separates southwest of Kyushu to form the YSWC which flows northward. After this, the KC inflows the Tsushima Strait with a current speed of 10-60 $cm\ s^{-1}$, and it then splits into three branches, one along the west coast of Japan, one along the continental shelf break and the last along the east coast of the Korean peninsula where it is called East Korean Warm Current (EKWC) which is present all year long. These current depictions are consistent with the triple-branch pattern introduced by *Ito et al.* [2014]. The EKWC separates from the coast at $37 - 38^{\circ}N$ generating the Ulleung Warm Eddy which is a warm eddy in the Ulleung Basin as is observed in Figure 9a with a size of $130\ \text{km} \times 220\ km$. The TSC, branches off the TC in the area west of the strait, then outflows from the Sea of Japan through the Tsugaru Strait, flowing southward along the Japanese coast into the North Pacific Ocean about 40-65 $cm\ s^{-1}$. The SY inflows into the Sea of Okhotsk from the Sea of Japan through the Soya/La Perouse Strait and flows southeastward along the Hokkaido coast as a coastal boundary current. The Liman Current flows from northeast to southwest along the Russian coast with a current speed of 10-35 $cm\ s^{-1}$, beginning at a latitude slightly north of Soya Strait, and terminating off Vladivostok.

The overall mean magnitude of this current is 27.74 $cm\ s^{-1}$, and the highest percentage of the mean magnitudes (15-20 $cm\ s^{-1}$) is about 14.7% (Figure 9b). The strongest current in the AOI is the KC, which has the dominant percentage of the higher magnitudes greater than 60 $cm\ s^{-1}$, about 90% of the total. In addition, current speeds in the Taiwan Strait, Tsushima Strait, Sea of Okhotsk, Tsugaru Strait and the Ulleung Basin are relatively higher at around 40 $cm\ s^{-1}$. In the Bohai Sea, Yellow Sea and north of the Sea of Japan, the mean magnitudes are lower at about 0 to 20 $cm\ s^{-1}$. Currents to the south of the AOI are discontinuous and have lower magnitudes.

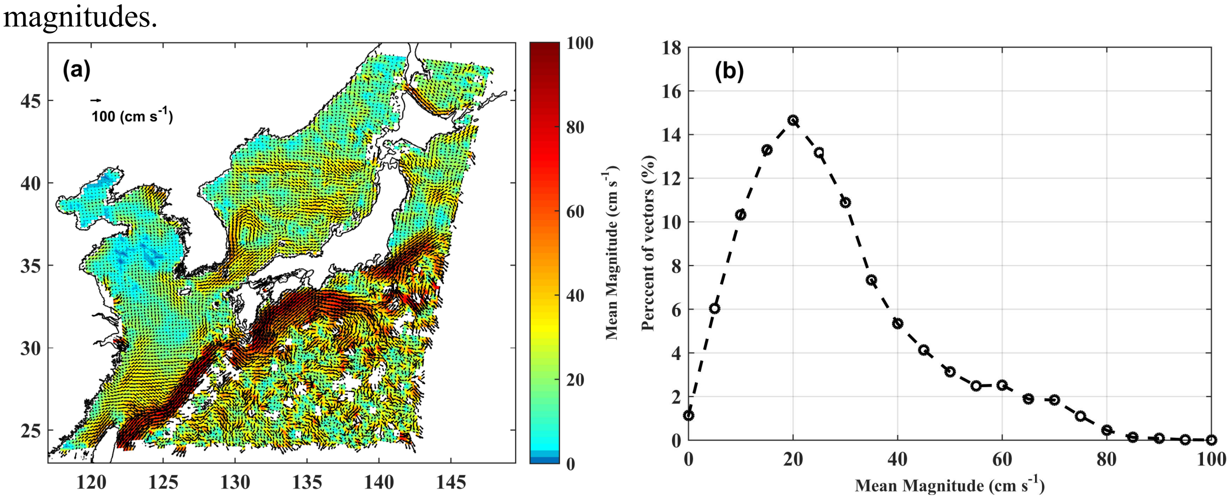

Figure 9. (a) Time-average mean flow from 5-year long MCC velocity fields. The color bar represents the mean magnitude of the currents. **(b)** Histogram of the distribution of the mean magnitude of the mean flow.

5.2 Seasonal MCC Velocity Fields Analysis

We also calculate the mean seasonal currents over the observation period to investigate the seasonal variations of the currents in the AOI. As there is a seasonal bias in the total number of vectors, the spatial coverage is different among the four seasons. To smooth and fill in the missing vectors, we employ optimal interpolation (OI) using the 5-year mean flow currents to compute the covariance function used in the OI mapping. More details on this procedure can be found in [*Wilkin et al.*, 2002]. The seasonal time-average flows are shown in Figure 10a-d. The OI method fills in the areas with no vectors based on the 5-year mean covariance function computed from MCC current vectors. OI mapping software also provides an estimate of the mean square error in the OI mapping procedure. As expected, spring has the best velocity coverage while winter has the poorest. The KC and SY are not observed in winter due to heavy cloud cover, resulting in the lack of MCC vectors in the Sea of Japan and north of the AOI. The consistent currents, KC, TWC, TSC, EKWC, SY and OY, are depicted clearly in spring, summer and fall. In addition, current speeds of these currents are higher in summer than in spring and fall. In addition, the TWC and TC also have lower current speeds in winter while the current speeds in summer are the highest. The China Coastal Current flows southward along the mainland China coast and forms during fall and winter while the TWC flows along the Taiwan coast. The Ulleung Warm Eddy is clearly captured in all four seasons and it exhibits clear seasonal variability. The Liman Current has higher current velocities in winter and fall than in spring and in summer because it is a cold current.

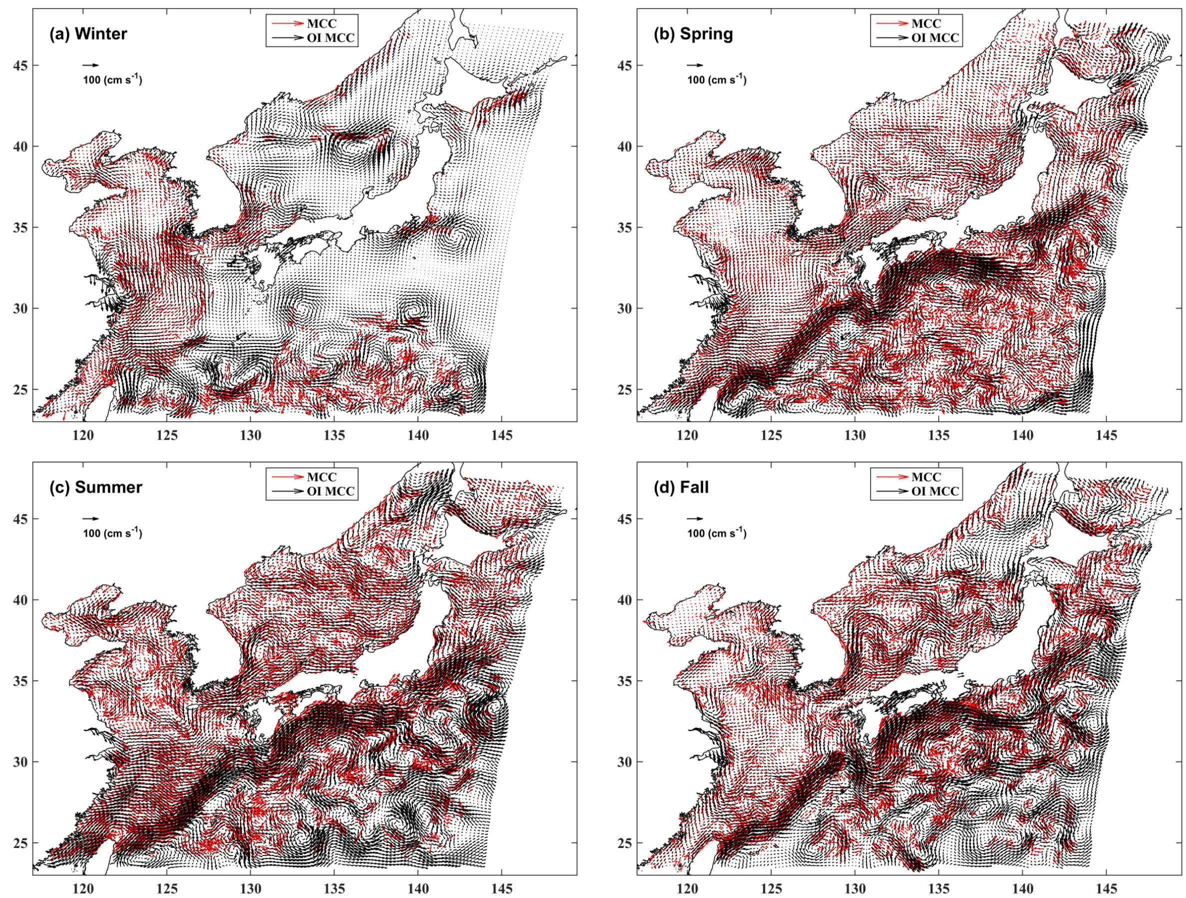

Figure 10. Seasonal mean flows, **(a)** winter, **(b)** spring, **(c)** summer and **(d)** fall over the 5−year observation period. The color bar represents the mean magnitude of the currents. The MCC vectors and OI MCC vectors are in red and black, respectively.

The Kuroshio south of Japan is well known to be in one of two persistent modes [*Rikiishi*, 1974], a small-meander mode which flows near the coast and a large-meander (LM) mode, in which the current axis is about 2° south of the Japanese coast at about $137^{\circ}E$ [*Taft*, 1972]. From the seasonal results in Figure 10, a meander is seen in spring, summer and fall. Given that the path of the Kuroshio meander has a large amplitude, we describe it as a LM. The amplitude and path of the Kuroshio meander vary in different seasons. Hence, the seasonal MCC average flows can be used to investigate the Kuroshio meander. In fact, our sequence of three weekly composite MCC current maps reveal clear changes in the Kuroshio meander over these three weeks.

5.3 Evolution of the Kuroshio Meander

Due to the high temporal resolution of the MCC currents derived from the GOCI images, we can have MCC current composite maps over relatively short time intervals such as 3-month, monthly and weekly. We can then explore the current changes over these time periods. In Figure 11a we show the 3-month MCC composites over the period from Mar. to May. in 2015. In the Kuroshio-Oyashio transition area, a WCR at center about $38^{\circ}N$ and $143^{\circ}E$ near the east coast of Japan was captured in Figure 11b-d. This Kuroshio WCR moves northward along Honshu from Mar. to May.. *Yasuda et al.* [1992] also revealed it sometimes moves northward and further northeastward along Hokkaido and Kuril Islands. This WCR gets stronger in these three weeks. The monthly MCC composites investigate the evolution of this WCR in this time period.

Using OI, we can obtain smooth surface current maps of the path of the Kuroshio, providing a new capability of investigating the KC both in space and time. The path of the KC varies significantly in these maps both in the south and in the north. Only the central part of the KC from southern Honshu up to the northeastern end of the meander does the KC appear to be very stable over this three months. The KC off central Japan has a LM, which varies over the 3 summer months of 2015. high path. In a recent study *Plotkin et al.* [2014], also revealed that this LM exhibits high path variability. In addition, we also investigated the variability of the LM in short time separation. In Figure 12 we present MCC current maps that show the space/time variability of this LM of the KC over three contiguous weeks. The LM starts moving eastward in the three weeks, accompanied by an anticyclonic eddy south of Honshu. Then a southward flow in the eastern part of the eddy carries the Kuroshio path offshore, creating the large meander. *Mitsudera et al.* [2001] and *Usui et al.* [2008] proved that anticyclonic eddies could influence the formation of the Kuroshio meander. Here we observed an anticyclonic eddy that significantly affected the phase speed and the amplitude of the meander in these three weeks in 2. Thus, with MCC currents compute from GOCI imagery, we can obtain the surface currents of the LM that reveal the temporal spatial changes of the KC LM that take place over a time period as short as three weeks. This is an entirely new approach to investigate the evolution of the Kuroshio and its meander in space and time.

6 Discussion and Conclusions

The MCC is an effective method to compute ocean currents from sequential satellite imagery, including but not limited to AVHRR, CZCS, MODIS, SeaWiFS, ERS-2 and Envisat SARs. However, all of these sensors are in polar orbit, which dictates a relatively long repeat time, while the GOCI is in geostationary orbit, with an hourly sampling interval and a ground resolution of 500 m, resulting in higher temporal and spatial resolutions, which have the advantage of being able to track smaller image features over the same time interval.

We automatically run MCC with sequential GOCI OC images with time spans of 1-7 h and 17-24 h. As the time interval increases, the processing time also increases dramatically.

Also, our AOI, the entire area covered by GOCI, is 5567×5685 pixels, indicating more processing time. In response, we introduce a novel search strategy to greatly improve the computational efficiency of the MCC searches. The results in Figure 5 demonstrate how the proposed method decreases 95.9% of the average processing time relative to the conventional MCC method when $V_R = 5\ cm\ s^{-1}$. This is done with little loss of accuracy and the number of vectors. We chose the GOCI OC products, Chl and Rrs555, as our inputs for the MCC computation. We routinely computed the ocean currents from GOCI OC imagery using the MCC method over a 5-year long time period from Jun. 1, 2011 to May. 31, 2016. The overall spatial distribution of the OC products, shown in Figure 4, reveals that the Chl and Rrs555 sequential images yield similar spatial coverage characteristics. This study provides strong evidence for the statistical analysis of the currents derived from GOCI using the MCC method. Due to cloud cover and weakly trackable features, the MCC fields have different spatial coverage. We calculate the daily and 7-day composites over the observation period (Figure 7) to analyze the vector distribution against time. The 7-day MCC composites have better spatial coverage over time. By making fusion of the Chl and Rrs555 derived composites, the spatial coverage of the MCC fields increases approximately 25%.

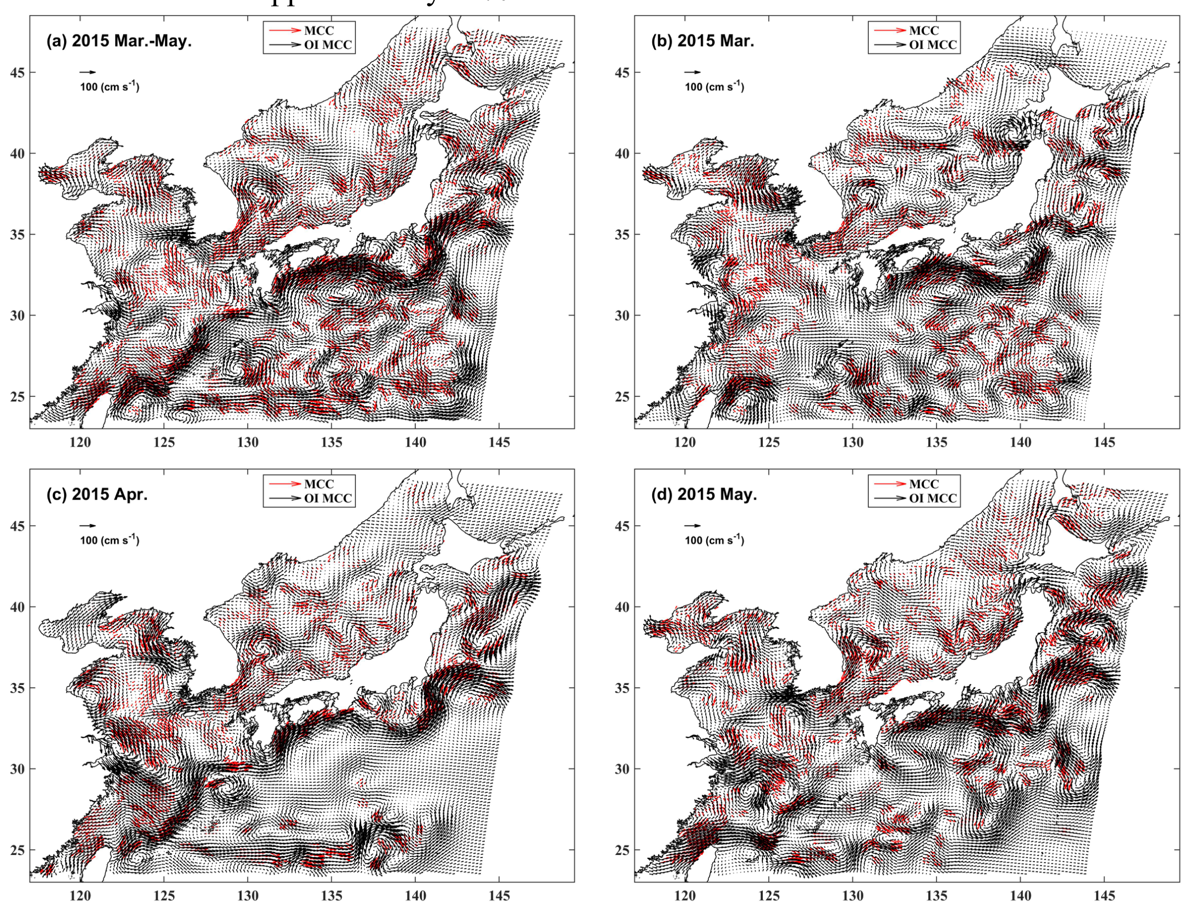

Figure 11. (a) 3-month MCC composites over from Mar. 2015 to May. 2015. Monthly MCC 00composites from **(b)** Mar., **(c)** Apr. and **(d)** May..

A 5-year mean flows are computed to investigate the major currents (Figure 9). We reveal the KC path, which is about 2,400 km long with a width from 100 km to 150 km. The TC originates from a branch of the KC. Then the TC outflows the Tsushima Strait forming the triple-branch pattern. The TWC, TSC, SY and OY are also investigated. In addition, the Ulleung Warm Eddy in the Ulleung Basin is the most obvious eddy in the mean flows. There is seasonal bias in the number of vectors, resulting in the seasonal vectors distribution differences. There are more vectors in spring and the fewest in winter. Seasonal time-average flows reveal seasonal current speed difference. Current speed in summer is higher than winter. Warm currents such as the KC, TWC and TC have higher current in summer while cold currents like Liman Current have higher current speed in winter. Figure 10e depicts the mean magnitude distribution of the seasonal mean flows. These results reveal that current speed in summer have higher percentage than other seasons.

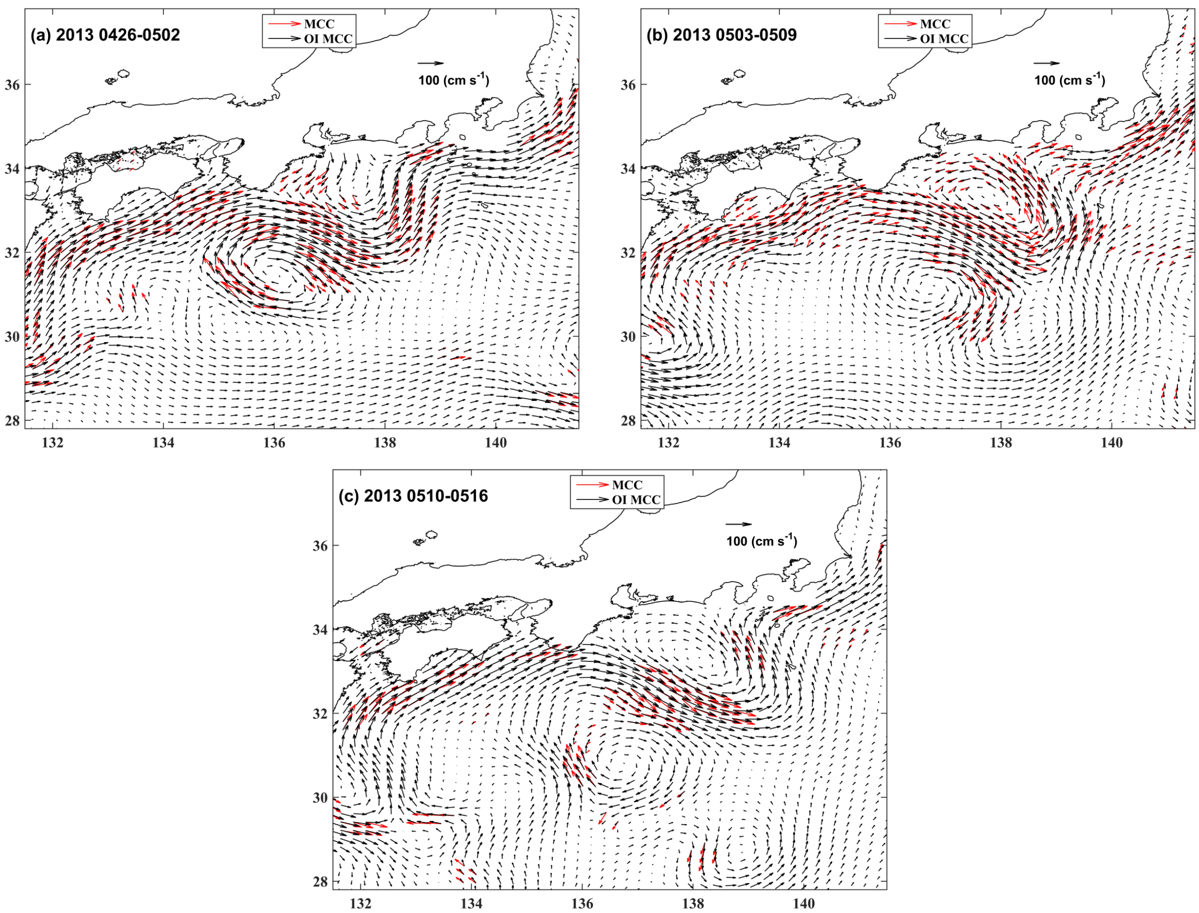

Figure 12. Weekly MCC composites of **(a)** Apr. 26 to May. 2 **(b)** May. 3 to May. 9 and **(c)** May. 10 to May. 16, 2013.

Using the 5-year mean MCC current map to compute our covariance function, we applied the OI method to fill the gaps in all MCC maps. Thus, we can obtain smooth monthly and weekly MCC composites with a high-resolution velocity coverage, providing the possibility of mapping surface current variability over short time separations. Using these types of surface currents maps we captured the evolution of the Kuroshio WCR near the east coast of Japan by the monthly MCC composites. Moreover, we also investigated the evolution of the Kuroshio meander over monthly and weekly time/space scales. The anticyclonic eddies significantly affect the phase speed and the amplitude of the meander, forcing the eastward propagation of the Kuroshio meander. This type of data analysis provides a new opportunity to study the formation of Kuroshio meander both in time and space. In addition to the KC LM there are a great many eddies that clearly form and dissipate in the study area. This type of surface current information could be very useful to marine users working in this area such as fishermen, search and rescue operations, and marine recreation.

In conclusion, the MCC method performs well when applied to sequential GOCI OC imagery with time intervals between 1-7 h and 17-24 h. By proposing a new search strategy, the computational efficiency of the MCC method is greatly improved. It has extraordinary significance for computing a large number of MCC currents over long observation period over a large area. Optimum interpolation can be effectively used to fill in missing MCC currents to gain a smooth map of sea surface currents. The overall spatial distribution of the OC products over the observation period provides evidence for the reasonable ocean current extraction with the MCC method. By making fusion of different MCC currents, the total spatial coverage increase approximately 25.6%. A 5-year mean and seasonal time-average flows are computed to study the major currents in the AOI. All these results proved the applicability of using the MCC method to investigate mesoscale currents in different temporal resolution in the AOI. Monthly and weekly OI interpolated MCC current maps clear demonstrated variability in the Kuroshio meander and in mesoscale eddies associated with the meander. This unique ability to depict high spatial resolution and short time scale changes in the surface currents of the region is unique and could be used for a great many marine applications requiring surface current information.

Acknowledgments

This work was supported in part by 863 High Technology Project of China under Grant 2012AA091701, in part by the National Natural Science Foundation of China under Grant 61401316, and in part by China Scholarship Council under Grant 201506270074. Thanks for Korea Ocean Satellite Center (KOSC), Korean Institute of Ocean Science and Technology (KIOST), NASA Goddard Space Flight Center, Ocean Ecology Laboratory and Ocean Biology Processing Group for support of the GOCI data.

References

References:

Abascal, A. J., S. Castanedo, R. Medina, I. J. Losada, and E. Alvarez-Fanjul (2009), Application of HF radar currents to oil spill modelling, *MAR POLLUT BULL*, *58*, 238-248, doi:10.1016/j.marpolbul.2008.09.020.

Andres, M., M. Wimbush, J. H. Park, K. I. Chang, B. H. Lim, D. R. Watts, H. Ichikawa, and W. J. Teague (2008), Observations of Kuroshio flow variations in the East China Sea, *Journal of Geophysical Research: Oceans*, *113*, C5013, doi:10.1029/2007JC004200.

Barrick, D. E., M. W. Evans, and B. L. Weber (1977), Ocean Surface Currents Mapped by Radar, *SCIENCE*, *198*, 138-144, doi:10.1126/science.198.4313.138.

Barrick, D. E. (1979), A coastal radar system for tsunami warning, *REMOTE SENS ENVIRON*, *8*, 353-358, doi:10.1016/0034-4257(79)90034-8.

Beardsley, R. C., R. Limeburner, H. Yu, and G. A. Cannon (1985), Discharge of the Changjiang (Yangtze river) into the East China sea, *CONT SHELF RES*, *4*, 57-76, doi:10.1016/0278-4343(85)90022-6.

Bowen, M. M., W. J. Emery, J. L. Wilkin, P. C. Tildesley, I. J. Barton, and R. Knewtson (2002), Extracting multiyear surface currents from sequential thermal imagery using the maximum cross-correlation technique, *J ATMOS OCEAN TECH*, *19*, 1665-1676, doi:10.1175/1520-0426(2002)019<1665:EMSCFS>2.0.CO;2.

Bowen, M. M., J. L. Wilkin, and W. J. Emery (2005), Variability and forcing of the East Australian Current, *Journal of Geophysical Research: Oceans*, *110*, C3019, doi:10.1029/2004JC002533.

Ciappa, A., L. Pietranera, A. Coletta, and X. Jiang (2010), Surface transport detected by pairs of COSMO-SkyMed ScanSAR images in the Qingdao region (Yellow Sea) during a macro-algal bloom in July 2008, *J MARINE SYST*, *80*, 135-142, doi:10.1016/j.jmarsys.2009.02.010.

Crocker, R. I., D. K. Matthews, W. J. Emery, and D. G. Baldwin (2007), Computing Coastal Ocean Surface Currents From Infrared and Ocean Color Satellite Imagery, *IEEE T GEOSCI REMOTE*, *45*, 435-447, doi:10.1109/TGRS.2006.883461.

Domingues, C. M., G. A. Gon Alves, R. D. Ghisolfi, and C. A. E. Garcia (2000), Advective Surface Velocities Derived from Sequential Infrared Images in the Southwestern Atlantic Ocean, *REMOTE SENS ENVIRON*, *73*, 218-226, doi:10.1016/S0034-4257(00)00096-1.

Dransfeld, S., G. Larnicol, and P. Y. Le Traon (2006), The Potential of the Maximum Cross-Correlation Technique to Estimate Surface Currents From Thermal AVHRR Global Area Coverage Data, *IEEE GEOSCI REMOTE S*, *3*, 508-511, doi:10.1109/LGRS.2006.878439.

Ebuchi, N., Y. Fukamachi, K. I. Ohshima, K. Shirasawa, M. Ishikawa, T. Takatsuka, T. Daibo, and M. Wakatsuchi (2006), Observation of the Soya Warm Current using HF ocean radar, *J OCEANOGR*, *62*, 47-61, doi:10.1007/s10872-006-0031-0.

Emery, W., M. Gade, and R. Romeiser (2006), Coastal ocean surface current retrievals from sequences of TerraSAR-X images, IEEE, 2006-01-01.

Emery, W. J., A. C. Thomas, M. J. Collins, W. R. Crawford, and D. L. Mackas (1986), An objective method for computing advective surface velocities from sequential infrared satellite images, *Journal of Geophysical Research: Oceans*, *91*, 12865-12878, doi:10.1029/JC091iC11p12865.

Emery, W. J., C. Fowler, and C. A. Clayson (1992), Satellite-image-derived Gulf Stream currents compared with numerical model results, *J ATMOS OCEAN TECH*, *9*, 286-304, doi:10.1175/1520-0426(1992)009<0286:SIDGSC>2.0.CO;2.

Garcia, C. A. E., and I. S. Robinson (1989), Sea surface velocities in shallow seas extracted from sequential coastal zone color scanner satellite data, *Journal of Geophysical Research: Oceans*, *94*, 12681-12691, doi:10.1029/JC094iC09p12681.

Georges, T. M., J. A. Harlan, and R. A. Lematta (1996), Large-scale mapping of ocean surface currents with dual over-the-horizon radars, *NATURE*, doi:10.1038/379434a0.

Hidaka, K. (1972), Oceanography in Japan, *NATURE*, *240*, 207-209, doi:10.1038/240207a0.

Hu, C., Z. Lee, and B. Franz (2012), Chlorophyllall algorithms for oligotrophic oceans: A novel approach based on three-band reflectance difference, *Journal of Geophysical Research: Oceans*, *117*, n/a-n/a, doi:10.1029/2011JC007395.

Ichikawa, H., and R. C. Beardsley (1993), Temporal and spatial variability of volume transport of the Kuroshio in the East China Sea, *Deep Sea Research Part I: Oceanographic Research Papers*, *40*, 583-605, doi:10.1016/0967-0637(93)90147-U.

Ichikawa, H., and R. C. Beardsley (2002), The current system in the Yellow and East China Seas, *J OCEANOGR*, *58*, 77-92, doi:10.1023/A:1015876701363.

Ito, M., A. Morimoto, T. Watanabe, O. Katoh, and T. Takikawa (2014), Tsushima Warm Current paths in the southwestern part of the Japan Sea, *PROG OCEANOGR*, *121*, 83-93, doi:10.1016/j.pocean.2013.10.007.

Ito, T., O. Togawa, M. Ohnishi, Y. Isoda, and T. Nakayama (2003), Variation of velocity and volume transport of the Tsugaru Warm Current in the winter of 1999 – 2000, *GEOPHYS RES LETT*, doi:10.1029/2003GL017522.

Kawamura, H., T. Ito, N. Hirose, T. Takikawa, and J. Yoon (2009), Modeling of the branches of the Tsushima Warm Current in the Eastern Japan Sea, *J OCEANOGR*, *65*, 439, doi:10.1007/s10872-009-0039-3.

Kelly, K. A., and P. T. Strub (1992), Comparison of velocity estimates from advanced very high resolution radiometer in the Coastal Transition Zone, *Journal of Geophysical Research: Oceans*, *97*, 9653-9668, doi:10.1029/92JC00734.

Matthews, D. K., and W. J. Emery (2009), Velocity observations of the California Current derived from satellite imagery, *Journal of Geophysical Research: Oceans*, *114*, C8001, doi:10.1029/2008JC005029.

Mitsudera, H., T. Waseda, Y. Yoshikawa, and B. Taguchi (2001), Anticyclonic eddies and Kuroshio Meander Formation, *GEOPHYS RES LETT*, *28*, 2025-2028, doi:10.1029/2000GL012668.

Nitani, H. (1972), *Beginning of the Kuroshio*,pp. 129-163, In: Stommel, H. and Yoshida, K. (eds.), Kuroshio: Its Physical Aspects., Tokyo, Japan: University of Tokyo press.

Ohshima, K. I., M. Wakatsuchi, Y. Fukamachi, and G. Mizuta (2002), Near-surface circulation and tidal currents of the Okhotsk Sea observed with satellite-tracked drifters, *Journal of Geophysical Research: Oceans*, *107*, 3195, doi:10.1029/2001JC001005.

Plotkin, D. A., J. Weare, and D. S. Abbot (2014), Distinguishing meanders of the Kuroshio using machine learning, *Journal of Geophysical Research: Oceans*, *119*, 6593-6604, doi:10.1002/2014JC010128.

Qazi, W. A., W. J. Emery, and B. Fox-Kemper (2014), Computing Ocean Surface Currents Over the Coastal California Current System Using 30-Min-Lag Sequential SAR Images, *IEEE T GEOSCI REMOTE*, *52*, 7559-7580, doi:10.1109/TGRS.2014.2314117.

Rajput, P., R. Ramakrishnan, and A. S. Rajawat (2014), Retrieval of coastal ocean currents using MCC technique on satellite imagery for supplementing altimeter derived currents, *The International Archives of Photogrammetry, Remote Sensing and Spatial Information Sciences*, *40*, 1483.

Rikiishi, K. (1974), Note on the Kuroshio meander, *Journal of the Oceanographical Society of Japan*, *30*, 42-45, doi:10.5928/kaiyou1942.30.42.

Roesler, C. J., W. J. Emery, and S. Y. Kim (2013), Evaluating the use of high-frequency radar coastal currents to correct satellite altimetry, *Journal of Geophysical Research: Oceans*, *118*, 3240-3259, doi:10.1002/jgrc.20220.

Ryu, J., H. Han, S. Cho, Y. Park, and Y. Ahn (2012), Overview of geostationary ocean color imager (GOCI) and GOCI data processing system (GDPS), *Ocean Science Journal*, *47*, 223-233, doi:10.1007/s12601-012-0024-4.

Semtner, A. J. (1995), Modeling Ocean Circulation, *SCIENCE*, *269*, 1379-1385, doi:10.1126/science.269.5229.1379.

Taft, B. (1972), *Characteristics of the flow of the Kuroshio south of Japan, in Kuroshio-Its Physical Aspects*, edited by H. Stommel and K. Yoshida ed.,pp. 165-216, Unvi. of Tokyo Press, Tokyo.

Takahashi, D., and A. Morimoto (2013), Mean field and annual variation of surface flow in the East China Sea as revealed by combining satellite altimeter and drifter data, *PROG OCEANOGR*, *111*, 125-139, doi:10.1016/j.pocean.2013.01.007.

Tokmakian, R., P. T. Strub, and J. McClean-Padman (1990), Evaluation of the maximum cross-correlation method of estimating sea surface velocities from sequential satellite images, *J ATMOS OCEAN TECH*, *7*, 852-865, doi:10.1175/1520-0426(1990)007<0852:EOTMCC>2.0.CO;2.

Usui, N., H. Tsujino, H. Nakano, and Y. Fujii (2008), Formation process of the Kuroshio large meander in 2004, *Journal of Geophysical Research: Oceans*, *113*, C8047, doi:10.1029/2007JC004675.

Wang, M., J. Ahn, L. Jiang, W. Shi, S. Son, Y. Park, and J. Ryu (2013), Ocean color products from the Korean Geostationary Ocean Color Imager (GOCI), *OPT EXPRESS*, *21*, 3835-3849, doi:10.1364/OE.21.003835.

Warren, M. A., G. D. Quartly, J. D. Shutler, P. I. Miller, and Y. Yoshikawa (2016), Estimation of ocean surface currents from maximum cross correlation applied to GOCI geostationary satellite remote sensing data over the Tsushima (Korea) Straits, *Journal of Geophysical Research: Oceans*, *121*, 6993-7009, doi:10.1002/2016JC011814.

Wilkin, J. L., M. M. Bowen, and W. J. Emery (2002), Mapping mesoscale currents by optimal interpolation of satellite radiometer and altimeter data, *OCEAN DYNAM*, *52*, 95-103, doi:10.1007/s10236-001-0011-2.

Yang, H., R. Arnone, and J. Jolliff (2015), Estimating advective near-surface currents from ocean color satellite images, *REMOTE SENS ENVIRON*, *158*, 1-14, doi:10.1016/j.rse.2014.11.010.

Yasuda, I., K. Okuda, and M. Hirai (1992), Evolution of a Kuroshio warm-core ring—variability of the hydrographic structure, *Deep Sea Research Part A. Oceanographic Research Papers*, *39*, S131-S161.